

# Single Spin Localization and Manipulation in Graphene Open-Shell Nanostructures

Jingcheng Li<sup>1</sup>, Sofia Sanz<sup>2</sup>, Martina Corso<sup>2,3</sup>, Deung Jang Choi<sup>2,3,5</sup>, Diego Peña<sup>4</sup>, Thomas Frederiksen<sup>2,5</sup>, Jose Ignacio Pascual<sup>1,5</sup>

<sup>1</sup> CIC nanoGUNE, 20018 Donostia-San Sebastián, Spain

<sup>2</sup>Donostia International Physics Center (DIPC), 20018 Donostia-San Sebastián, Spain

<sup>3</sup> Centro de Física de Materiales CFM/MPC (CSIC-UPV/EHU), 20018 Donostia-San Sebastián, Spain

<sup>4</sup>Centro Singular de Investigación en Química Biolóxica e Materiais Moleculares (CiQUS), and Departamento de Química Orgánica, Universidade de Santiago de Compostela, Spain

<sup>5</sup>Ikerbasque, Basque Foundation for Science, 48013 Bilbao, Spain

April 7, 2024

**Predictions state that graphene can spontaneously develop magnetism from the Coulomb repulsion of its  $\pi$ -electrons, but its experimental verification has been a challenge. Here, we report on the observation and manipulation of individual magnetic moments localized in graphene nanostructures on a Au(111) surface. Using scanning tunneling spectroscopy, we detected the presence of single electron spins localized around certain zigzag sites of the carbon backbone via the Kondo effect. Two near-by spins were found coupled into a singlet ground state, and the strength of their exchange interaction was measured via singlet-triplet inelastic tunnel electron excitations. Theoretical simulations demonstrate that electron correlations result in spin-polarized radical states with the experimentally observed spatial distributions. Hydrogen atoms bound to these radical sites quench their magnetic moment, permitting us to switch the spin of the nanostructure using the tip of the microscope.**

Among the many applications predicted for graphene, its use as a source of magnetism is the most unexpected one, and an attractive challenge for its active role in spintronic devices <sup>1</sup>. Generally, magnetism is associated to a large degree of electron localization and strong spin-orbit interaction. Both premises are absent in graphene, a strongly diamagnetic material. The simplest method to induce magnetism in graphene is to create an imbalance in the number of carbon atoms in each of the two sublattices, what, according to the Lieb's theorem for bipartite lattices <sup>2</sup>, causes a spin imbalance in the system. This can be done by either inserting defects that remove a single  $p_z$  orbital <sup>3-6</sup> or by shaping graphene with zigzag edges <sup>7,8</sup>. However, magnetism can also emerge in graphene nanostructures where Lieb's theorem does not apply <sup>9,10</sup>. For example, in  $\pi$ -conjugated systems with small band gaps, Coulomb repulsion between valence electrons forces the electronic system to reorganize into open-shell configurations <sup>11</sup> with unpaired electrons (radicals) localized at different atomic sites. Although the net magnetization of the nanostructures may be zero, each radical state hosts a magnetic moment of size  $\mu_B$ , the Bohr magneton, turning the graphene nanostructure paramagnetic. This basic principle predicts, for example, the emergence of edge magnetization originating from zero-energy modes in sufficiently wide zigzag <sup>12-14</sup> and chiral <sup>15,16</sup> graphene nanoribbons (GNRs).

The experimental observation of spontaneous magnetization driven by electron correlations is still challenging, because, for example, atomic defects and impurities in the graphene structures <sup>17,18</sup> hide the weak paramagnetism of radical sites <sup>19</sup>. Scanning probe microscopies can spatially localize the source states of magnetism, but they require both atomic-scale resolution and spin-sensitive measurements. Here we achieve these conditions to demonstrate that atomically-defined graphene nanostructures can host localized spins at specific sites and give rise to the Kondo effect <sup>20,21</sup>, a many-body phenomenon caused by the interaction between a localized spin and free conduction electrons in its proximity. Using a low-temperature scanning tunneling microscope (STM) we use this signal to map the spin localization within the nanostructure and to detect spin-spin interactions.

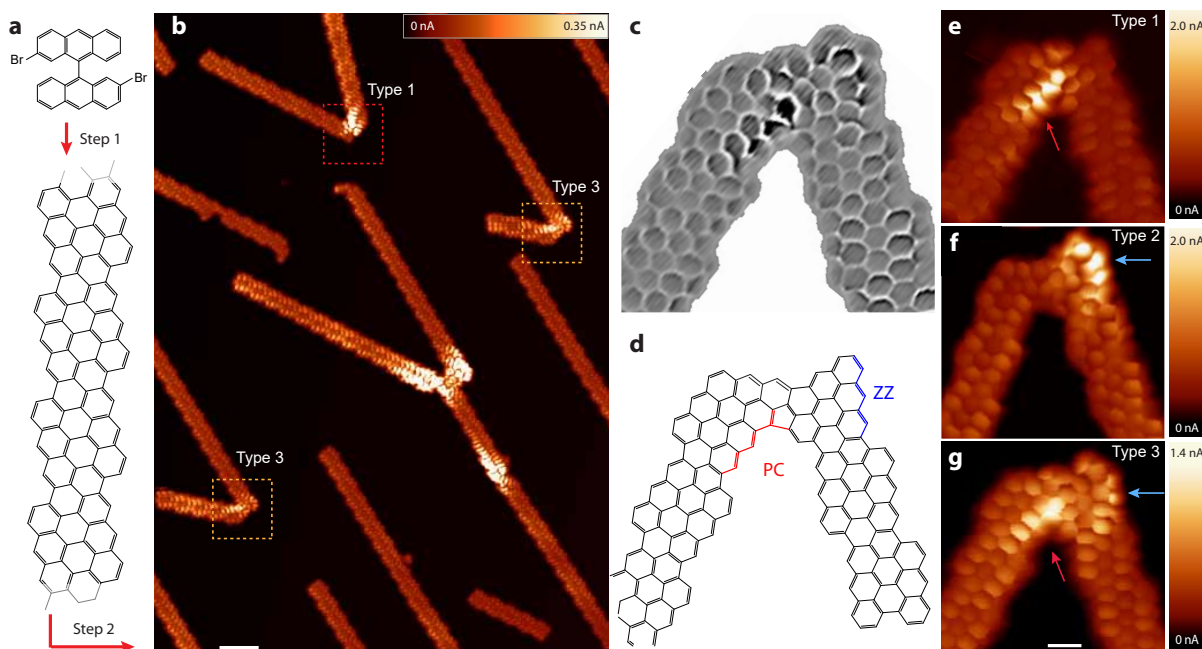


**Figure 1: Formation of graphene junctions by cross-dehydrogenative coupling of adjacent graphene nanoribbons.** **a**, Model structures of the organic precursor 2,2'-dibromo-9,9'-bianthracene and of the on-surface synthesized (3,1)chGNR after Ullmann-like C-C coupling reaction and cyclodehydrogenation on Au(111). **b**, Constant-height current images ( $V = 2$  mV, scale bar: 2 nm) showing joint chGNR nanostructures, with an angle of  $\sim 50^\circ$ , obtained after further annealing the sample. A CO-functionalized tip was used to resolve the chGNR ring structure. Dashed boxes indicate the most characteristic chGNR junctions, whose structure is shown in panels **c,d**. **c**, Laplace-filtered image of the junction shown in panel **g** to enhance the backbone structure, and **d**, model structure of the junction. PC labels the pentagonal cove site and the ZZ the zigzag site. **e-g**, Constant-height current images ( $V = 8$  mV, scale bar 0.5 nm) of the three types of chGNR junctions with same backbone structures but with different LDOS distribution.

The graphene nanostructures studied here are directly created on a Au(111) surface by cross-dehydrogenative coupling of adjacent chiral GNRs (chGNRs)<sup>22</sup>. We deposited the organic molecular precursors 2,2'-dibromo-9,9'-bianthracene (Fig. 1a) on a clean Au(111) surface, and annealed stepwisely to 250 °C (step 1 in Fig. 1a) to produce narrow chGNRs<sup>14,23</sup>. The chiral ribbons are semiconductors with a band-gap of 0.7 eV (Supplementary Figs. S7 and S8) and show two enantiomeric forms on the surface<sup>24</sup>. By further annealing the substrate to 350 °C (step 2 in Fig. 1a), chGNRs fuse together into junctions, as shown in Fig. 1b. The chGNR junctions highlighted by dashed rectangles are the most frequently found in our experiments. They consist of two chGNRs with the same chirality linked together by their termination (Fig. 1c). The creation of this stable nanostructure implies the reorganization of the carbon atoms around the initial contact point<sup>25</sup> into the final structure shown in Fig. 1d, as described in Supplementary Fig. S1.

In Fig. 1b, certain regions of the junctions appear brighter when recorded at low sample bias, reflecting enhancements of the local density of states (LDOS) close to the Fermi level. Interestingly, the precise location of the bright regions is not unique, but can be localized over the pentagon cove (PC) site (Type 1, Fig. 1e), over the terminal zigzag (ZZ) site of the junction (Type 2, Fig. 1f), or over both (Type 3, Fig. 1g). Despite these different LDOS distributions in the three types of junctions, they have identical carbon arrangement (Fig. 1d).

To understand the origin of the enhanced LDOS at the ZZ and PC sites, we recorded differential conductance spectra ( $dI/dV$ ) on the three types of junctions. Spectra on the bright sites of Type 1 and 2 junctions show very pronounced zero-bias peaks (Fig. 2a,b) localized over the bright sites (spectra 1 to 4, and 6 to 8), and vanishing rapidly in neighbor rings (spectra 5, 9, and 10). These are generally ascribed as Abrikosov-Suhl resonances due to the Kondo effect, and named as Kondo resonances<sup>20,21</sup>. Their observation is a proof of a localized magnetic moment screened by conduction electrons<sup>26,27</sup>. The resonance line width increases with temperature (Fig. 2d) and magnetic field (Fig. 2e) following the characteristic behavior of a spin-1/2

system with a Kondo Temperature  $T_K \sim 6 \text{ K}$ <sup>27,28</sup>.

Junctions with two bright regions (Type 3) show different low-energy features: two peaked steps in  $dI/dV$  spectra at  $\sim \pm 10 \text{ meV}$  (Fig. 2c). The peaks appear at the same energies over the terminal ZZ segment and over the PC region for a given nanostructure, and vanish quickly away from these sites. Based on the existence of localized spins on bright areas of Type 1 and 2 junctions, we attribute the double-peak features to excitation of two exchange coupled spins localized at each junction site. The exchange interaction tends to freeze their relative orientation, in this case antiferromagnetically into a singlet ground state. Electrons tunneling into the coupled spin system can excite a spin reversal in any of them when their energy equals the exchange coupling energy between the spins, i.e.,  $eV \geq J$ . Usually, this inelastic process is revealed in  $dI/dV$  spectra as steps at the onset of spin excitations<sup>31</sup>, from which one can directly determine the strength of the exchange coupling  $J$  between the spins. Here, the spectra additionally show asymmetric peaks on top of the excitation onsets characteristic of Kondo-like systems with particle-hole asymmetry, when spin fluctuations are hindered in the ground state<sup>30,32-34</sup>. Hence, the gap between  $dI/dV$  peaks in Fig. 2c is a measure of the interaction strength between the two localized spins.

Interestingly, the spectral gap in Type 3 junctions increases with the length of the connecting ribbons (See Supplementary Fig. 15b). In Fig. 2f we compare low-energy spectra of two junctions with different chGNR lengths. Although the atomic structures of both junctions are identical, the one with shorter ribbons (upper curve; 9 and 2 precursor units) displays a smaller gap than the junction of longer chGNRs (lower curve; > 8 and 7 units). Fitting the spectra with a model of two coupled spin- $1/2$  systems<sup>30</sup>, one obtains the exchange coupling  $J = 2.7$  (9.9) meV for the upper (lower) spectrum.

To explain the emergence of localized spins, we simulated the spin-polarized electronic structure of chGNR junctions using both density functional theory (DFT) and mean-field Hub-

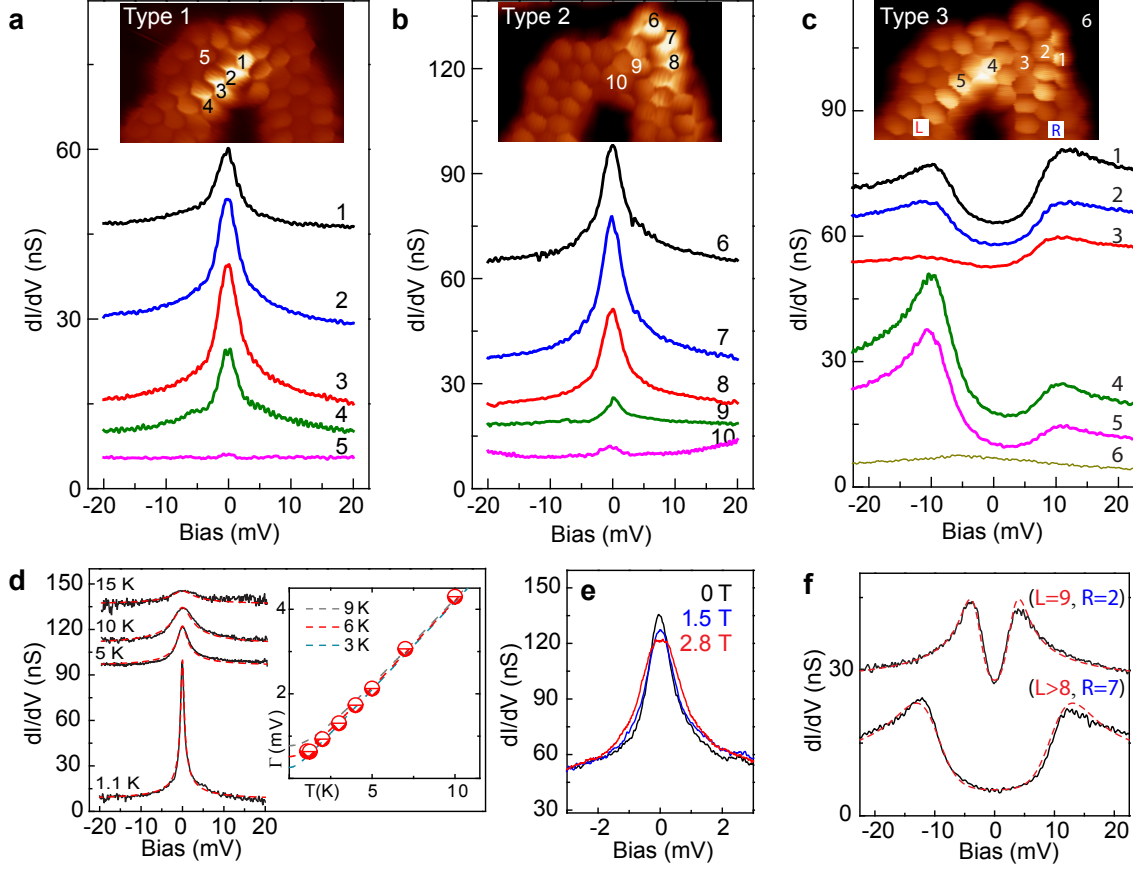


**Figure 2: Spatial distribution of Kondo resonances and singlet-triplet excitations in chGNR junctions.** **a,b**, Kondo resonances over the bright regions of Type 1 and Type 2 junctions, respectively. The zero-bias peaks are mostly detected over four PC rings of Type 1 junctions and over three ZZ rings of Type 2 junctions. **c**, Double-peak features around zero bias over Type 3 junctions. **d**, Temperature dependence of the Kondo resonance. All spectra were measured over the same PC site. The full width at half maximum (FWHM) at each temperature is extracted by fitting a Frota function (red dashed lines)<sup>29</sup>, and corrected for the thermal broadening of the tip<sup>27</sup>. The temperature dependence of FWHM was fit by the empirical expression  $\sqrt{(\alpha k_B T)^2 + (2k_B T_K)^2}$ <sup>28</sup>, resulting in a Kondo temperature  $T_K \sim 6$  K and  $\alpha = 9.5$ . **e**, Magnetic field dependence of a Kondo resonance (over the same PC site) at the field strengths indicated in the figure. **f**, Split-peak  $dI/dV$  features for nanostructures with different sizes, determined by the number of precursor units in each chGNR, labeled L and R in panel c. The gap width increases with the length of the ribbons (Supplementary Section 7). The red dashed lines are fits to our spectra using a model for two coupled spin- $1/2$  systems<sup>30</sup>. The spectra in **d** and **e** were acquired with a metal tip, while the others with a CO-terminated tip.

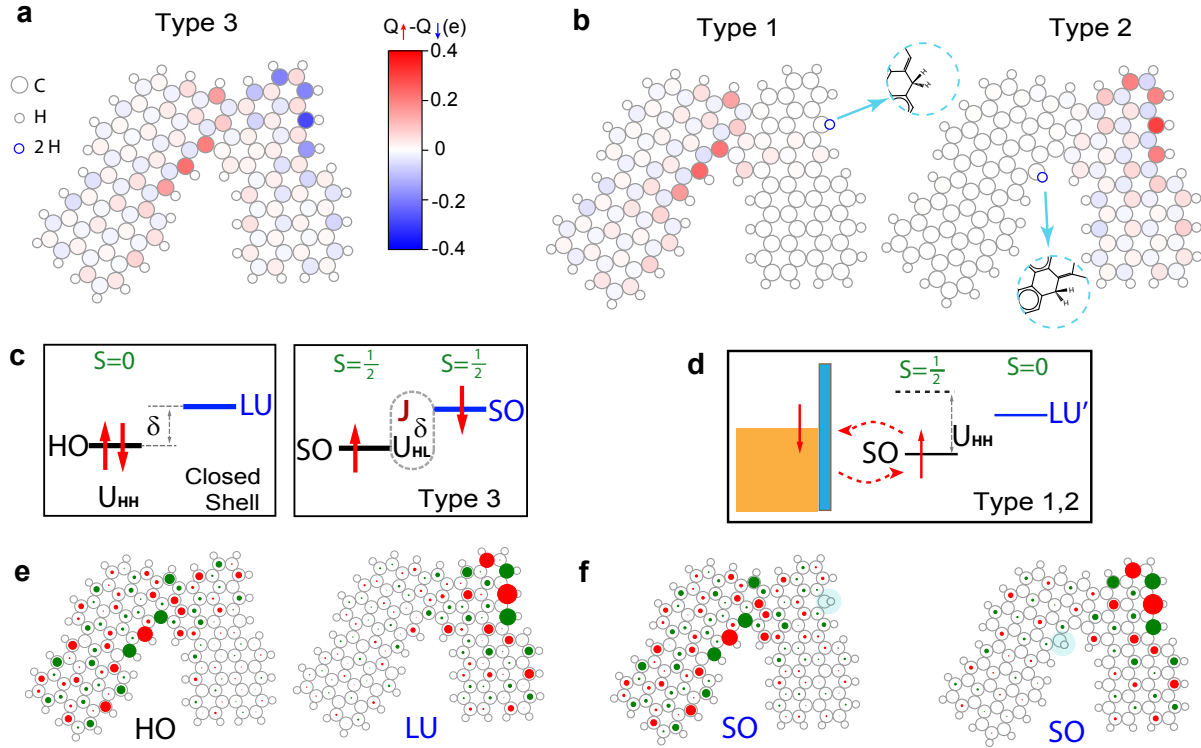


**Figure 3: Calculated electronic states of chGNR junctions.** **a,b**, Spin polarization obtained from DFT simulations in a Mulliken population analysis. The standard junction shown in **a** (all peripheral carbons bonded to H) shows spontaneous spin localization in both PC and ZZ regions, revealing the apparition of radical states. Adding a H atom to an external carbon in either the ZZ (Type 1) or PC (Type 2) removes the corresponding radical state and, hence, its spin-polarization. **c**, Schema of the spontaneous spin polarization when one of the two electrons in the HO level gets promoted to the LU level to form two separated, exchange coupled spin- $\frac{1}{2}$  systems (Type 3 junction). This process is energetically favored when the reduction in Coulomb energy  $U_{HH} - U_{HL}$  plus exchange energy  $J$  exceeds the level separation  $\delta$ , i.e.,  $\delta + U_{HL} - J < U_{HH}$ . **d**, Sketch of the spin- $\frac{1}{2}$  Kondo state generated with a single radical (Type 1 and 2 junctions). **e**, Single-particle TB wave functions (HO/LU) for Type 3 junction. **f**, Single-particle TB wave functions (SO) for Type 1 and Type 2 junctions. Red-green colors represent the positive-negative phase.

bard (MFH) models (see Supplementary Sections 5 and 6). Fig. 3a shows the spin-polarization of a junction of Fig. 1d. The ground state exhibits a net spin localization at the ZZ and PC regions with opposite sign, which is absent in the bare ribbons. This spin distribution agrees with the observations for Type 3 junctions. The origin of the spontaneous magnetization can be rationalized by considering the effect of Coulomb correlations between  $\pi$ -electrons as described within a tight-binding (TB) model. The spin distribution is related to the appearance of two junction states inside the gap of the (3,1)-chGNR electronic bands, localized at the PC and ZZ sites, respectively. In the absence of electron-electron correlations, these two states conform the highest occupied (HO) and lowest unoccupied (LU) molecular states of the nanostructure (Fig. 3e). Due to the large degree of localization (Supplementary Figs. S10-S11), the Coulomb repulsion energy  $U_{\text{HH}}$  between two electrons in the HO state becomes comparable with the energy difference  $\delta$  between the two localized levels. Hence, in a simplified picture, the two electrons find a lower-energy configuration by occupying each a different, spatially separated in-gap state. These two states become singly occupied (SO), spin-polarized (i.e., they have a net magnetic moment), and exchange coupled as schematically illustrated in Fig. 3c. Similar conclusions regarding the emergence of radical states at PC and ZZ sites can also be reached using the empirical Clar’s aromatic  $\pi$ -sextet rule (Supplementary Section 3).

According to both DFT (Fig. 3a) and MFH (Supplementary Fig. S9) the magnetic moments are antiferromagnetically aligned into a singlet ground state. Therefore, the inelastic features in  $dI/dV$  spectra found over Type 3 junctions (Fig. 2c) are associated to singlet-triplet excitations induced by tunneling electrons. In fact, the smaller excitation energy found for the smaller ribbons in both theory and experiment (Supplementary Section 7) agrees with a weaker exchange interaction due to a larger localization of the spin-polarized states. Alternative scenarios for peaks around  $E_F$ , such as single-particle states or Coulomb-split radical states<sup>6</sup>, would show the opposite trend with the system size.

To account for spin localization in only one of the two radical regions in Type 1 and 2



junctions, one of the two edge magnetic moments has to vanish. H-passivation of radical sites is a highly probable process occurring on the surface due to the large amount of hydrogen available during the reaction<sup>35</sup>. DFT simulations show that attaching an extra H atom into an edge carbon in either the ZZ (Type 1) or PC (Type 2) sites leads to its  $sp^3$  hybridization and the removal of a  $p_z$  orbital from the aromatic backbone. This completely quenches the magnetic moment of the passivated region, and leaves the junction with a single electron localized at the opposite radical site (Supplementary Fig. S6). The computed distributions for the two energetically most favorable adsorption sites (Fig. 3b) are in excellent agreement with the extension of the Kondo resonance mapped in Fig. 2a,b.

The presence of extra H atoms in Type 1 and 2 junctions was confirmed by electron induced H-atom removal experiments. Figure 4 a shows a structure formed by three chGNRs connected via Type 1 and 2 junctions. Accordingly, their  $dI/dV$  spectra (black curves in Figs. 4c,d) show a Kondo resonance at the  $PC_1$  and  $ZZ_2$  regions. We placed the STM tip on top of the opposite sites  $ZZ_1$  and  $PC_2$ , and raised the positive sample bias well above 1 V. A step-wise decrease of the tunneling current indicated the removal of the extra H atom (inset in Fig. 4c). The resulting junction appeared with double bright regions in low-bias images (Fig. 4b), and the  $PC_1$  and  $ZZ_2$  spectra turned into  $dI/dV$  steps characteristic of Type 3 junctions (blue curves in Figs. 4c,d). Thus, the removal of H atoms activated the magnetic moment of the initially unpolarized  $ZZ_1$  and  $PC_2$  sites, converting Type 1 and 2 junctions into Type 3, and switching the total spin of the junction from spin  $1/2$  to zero.

The magnetic state of the junction was also changed by creating a contact between the STM tip apex and a radical site. In the experiments shown in Figure 5, the STM tip was approached to the ZZ sites of a Type 3 junction. A step in the conductance-distance plot (Fig. 5b) indicated the formation of a contact. The created tip-chGNR contact could be stretched up to 3 Å before breaking (retraction step in Fig. 5b), signaling that a chemical bond was formed.  $dI/dV$  spectra recorded before the bond formation (black point in Fig. 5c) shows the split-peak

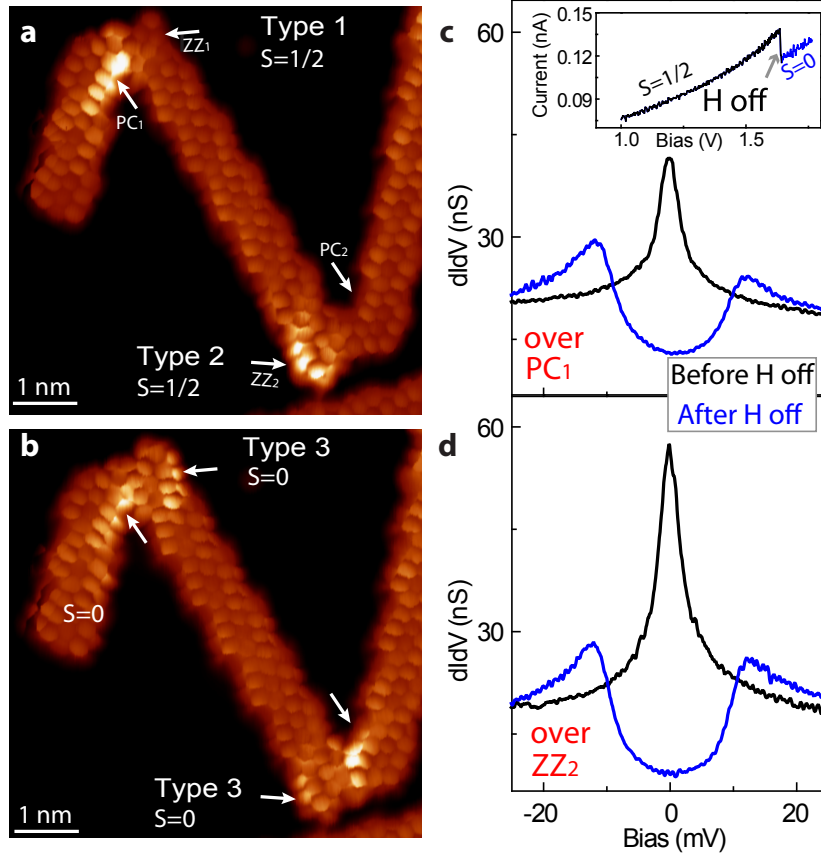


Figure 4: **Spin manipulation by electron-induced removal of extra H-atoms.** **a**, Constant-height current image of two junctions with extra H atoms ( $V = 8$  mV). **b**, Image with same conditions as in **a** after the removal of the extra H-atoms induced by tunneling electrons. The dehydrogenation processes were done over the  $ZZ_1$  and  $PC_2$  sites. **c,d**,  $dI/dV$  spectra taken over  $PC_1$  and  $ZZ_2$  regions (indicated in **a** and **b** respectively) before (black) and after (blue) the dehydrogenation processes. Inset in **c** shows the current during the process of dehydrogenation.

feature of Type 3 junctions (black spectrum in Fig. 5c). After the bond formation (blue and red points in Fig. 5b), the spectra changed to show Kondo resonances (blue and red spectra in Fig. 5c), persisting during contact retraction until the bond-breaking step, where double-peak features are recovered (green spectrum in Fig. 5c). The formation of a tip-chGNR bond thus removed the spin of the  $ZZ$  site, and the transport spectra reflect the Kondo effect due to the remaining spin embedded in the junction. If the STM tip contacts instead the  $ZZ$  radical site

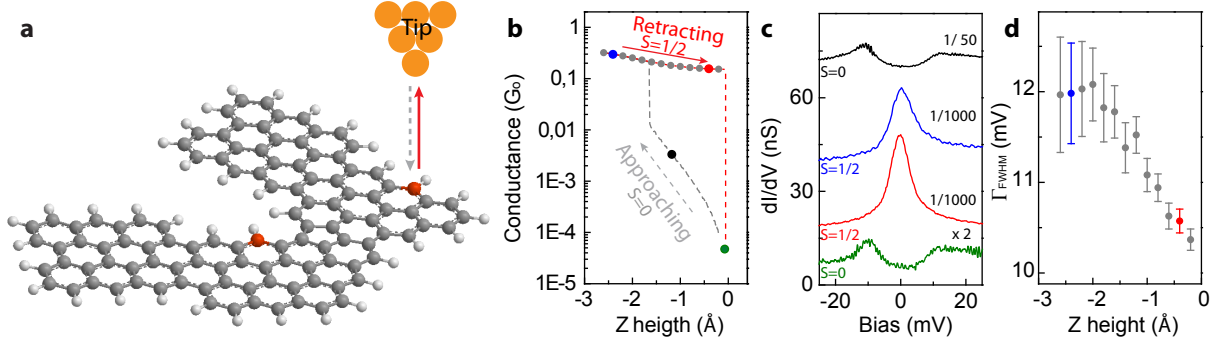


Figure 5: **Kondo effect from the spin embedded in a lifted chGNR junction.** **a**, Schematics of the process where the tip of the STM is first approached to the ZZ site of a Type 3 junction (gray dashed arrow) and then retracted to lift the junction away from the substrate (red arrow), resulting in a suspended junction between tip and substrate. **b**, Simultaneously recorded conductance curve ( $V = -50$  mV) during the approach, jump to contact and lift processes. **c**,  $dI/dV$  spectra recorded at the specific heights indicated with colored points on the curves in **b**. **d**, Full widths at half maximum (FWHM) of spectra acquired in the retraction process (points in **c**), extracted from a fit using the Frota function<sup>29</sup>.

of a Type 2 junction (shown in Supplementary Section 4) the initial Kondo resonance disappears from the spectra, signaling the complete demagnetization of the junction. The width of the Kondo resonance in the contacted junctions (blue and red plots in Fig. 5c) is significantly larger than in Type 1 and 2 cases, probably because it incorporates scattering with tip states<sup>36,37</sup>, and monotonously narrows as the contact is pulled apart (Fig. 5d). The survival of the Kondo effect in the contacted Type 3 junctions is a remarkable outcome of our experiments, which demonstrate the addressability of such localized magnetic moments in graphene nanostructure devices.

## Reference

1. Han, W., Kawakami, R. K., Gmitra, M. & Fabian, J. Graphene spintronics. *Nat. Nanotechnol.* **9**, 794–807 (2014).

2. Lieb, E. H. Two theorems on the hubbard model. *Phys. Rev. Lett.* **62**, 1201 (1989).
3. Yazyev, O. V. & Helm, L. Defect-induced magnetism in graphene. *Phys. Rev. B* **75**, 125408 (2007).
4. Nair, R. R. *et al.* Spin-half paramagnetism in graphene induced by point defects. *Nat. Phys.* **8**, 199–202 (2012).
5. McCreary, K. M., Swartz, A. G., Han, W., Fabian, J. & Kawakami, R. K. Magnetic Moment Formation in Graphene Detected by Scattering of Pure Spin Currents. *Phys. Rev. Lett.* **109**, 186604 (2012).
6. Gonzalez-Herrero, H. *et al.* Atomic-scale control of graphene magnetism by using hydrogen atoms. *Science* **352**, 437–441 (2016).
7. Fernández-Rossier, J. & Palacios, J. J. Magnetism in Graphene Nanoislands. *Phys. Rev. Lett.* **99**, 177204 (2007).
8. Yazyev, O. V. Emergence of magnetism in graphene materials and nanostructures. *Rep. Prog. Phys.* **73**, 056501 (2010).
9. Alexandre, S. S., Lúcio, A. D., Castro Neto, A. H. & Nunes, R. W. Correlated magnetic states in extended one-dimensional defects in graphene. *Nano Lett.* **12**, 5097–5102 (2012).
10. Ortiz, R., Lado, J. L., Melle-Franco, M. & Fernández-Rossier, J. Engineering spin exchange in nonbipartite graphene zigzag edges. *Phys. Rev. B* **94**, 094414 (2016).
11. Morita, Y., Suzuki, S., Sato, K. & Takui, T. Synthetic organic spin chemistry for structurally well-defined open-shell graphene fragments. *Nat. Chem.* **3**, 197–204 (2011).
12. Son, Y.-W., Cohen, M. L. & Louie, S. G. Half-Metallic Graphene Nanoribbons. *Nature* **444**, 347–350 (2006).

13. Tao, C. *et al.* Spatially Resolving Spin-split Edge States of Chiral Graphene Nanoribbons. *Nat. Phys.* **7**, 616–620 (2011).
14. Ruffieux, P. *et al.* On-surface synthesis of graphene nanoribbons with zigzag edge topology. *Nature* **531**, 489–492 (2016).
15. Yazyev, O. V., Capaz, R. B. & Louie, S. G. Theory of magnetic edge states in chiral graphene nanoribbons. *Phys. Rev. B* **84**, 115406 (2011).
16. Carvalho, A. R., Warnes, J. H. & Lewenkopf, C. H. Edge magnetization and local density of states in chiral graphene nanoribbons. *Phys. Rev. B* **89**, 245444 (2014).
17. Sepioni, M. *et al.* Limits on intrinsic magnetism in graphene. *Phys. Rev. Lett.* **105**, 207205 (2010).
18. Nair, R. R. *et al.* Dual origin of defect magnetism in graphene and its reversible switching by molecular doping. *Nat. Commun.* **4**, 1–6 (2013).
19. Červenka, J., Katsnelson, M. I. & Flipse, C. F. J. Room-temperature ferromagnetism in graphite driven by two-dimensional networks of pointdefects. *Nat. Phys.* **5**, 840–844 (2009).
20. Kondo, J. Resistance Minimum in Dilute Magnetic Alloys. *Prog. Theor. Phys.* **32**, 37–49 (1964).
21. Ternes, M., Heinrich, A. J. & Schneider, W.-D. Spectroscopic manifestations of the Kondo effect on single adatoms. *J. Phys.: Condens. Matter* **21**, 053001 (2009).
22. Dienel, T. *et al.* Resolving Atomic Connectivity in Graphene Nanostructure Junctions. *Nano Lett.* **15**, 5185–5190 (2015).
23. de Oteyza, D. G. *et al.* Substrate-independent growth of atomically precise chiral graphene nanoribbons. *ACS Nano* **10**, 9000–9008 (2016).

24. Merino-Díez, N. *et al.* Unraveling the electronic structure of narrow atomically precise chiral graphene nanoribbons. *J. Phys. Chem. Lett.* **9**, 25–30 (2018).
25. Shiotari, A. *et al.* Strain-induced skeletal rearrangement of a polycyclic aromatic hydrocarbon on a copper surface. *Nat. Commun.* **8**, 16089 (2017).
26. Fernández-Torrente, I., Franke, K. J. & Pascual, J. I. Vibrational Kondo Effect in Pure Organic Charge-Transfer Assemblies. *Phys. Rev. Lett.* **101**, 217203 (2008).
27. Zhang, Y.-h. *et al.* Temperature and magnetic field dependence of a kondo system in the weak coupling regime. *Nat. Commun.* **4**, 2110 (2013).
28. Nagaoka, K., Jamneala, T., Grobis, M. & Crommie, M. F. Temperature Dependence of a Single Kondo Impurity. *Phys. Rev. Lett.* **88**, 77205 (2002).
29. Frota, H. O. Shape of the Kondo resonance. *Phys. Rev. B* **45**, 1096–1099 (1992).
30. Ternes, M. Spin excitations and correlations in scanning tunneling spectroscopy. *New J. Phys.* **17**, 63016 (2015).
31. Hirjibehedin, C. F., Lutz, C. P. & Heinrich, A. J. Spin coupling in engineered atomic structures. *Science* **312**, 1021–1024 (2006).
32. Heersche, H. B. *et al.* Kondo effect in the presence of magnetic impurities. *Phys. Rev. Lett.* **96**, 017205 (2006).
33. Paaske, J. *et al.* Non-equilibrium singlet-triplet kondo effect in carbon nanotubes. *Nat. Phys.* **2**, 460–464 (2006).
34. Ortiz, R., García-Martínez, N. A., Lado, J. L. & Fernández-Rossier, J. Electrical spin manipulation in graphene nanostructures. *arXiv:1712.97282v1* .
35. Talirz, L. *et al.* Termini of Bottom-Up Fabricated Graphene Nanoribbons. *J. Am. Chem. Soc.* **135**, 2060–2063 (2013).

36. Jasper-Tönnies, T. *et al.* Conductance of a Freestanding Conjugated Molecular Wire. *Phys. Rev. Lett.* **119**, 066801 (2017).
37. Choi, D.-J., Abufager, P., Limot, L. & Lorente, N. From tunneling to contact in a magnetic atom: The non-equilibrium kondo effect. *J. Chem. Phys.* **146**, 092309 (2017).
38. Soler, J. M. *et al.* The siesta method for ab initio order-n materials simulation. *J. Phys.: Condens. Matter* **14**, 2745–2779 (2002).
39. Ceperley, D. M. & Alder, B. J. Ground state of the electron gas by a stochastic method. *Phys. Rev. Lett.* **45**, 566–569 (1980).
40. Perdew, J. P., Burke, K. & Ernzerhof, M. Generalized gradient approximation made simple. *Phys. Rev. Lett.* **77**, 3865–3868 (1996).
41. Hancock, Y., Uppstu, A., Saloriutta, K., Harju, A. & Puska, M. J. Generalized tight-binding transport model for graphene nanoribbon-based systems. *Phys. Rev. B* **81**, 245402 (2010).

## Methods

**Sample preparation and experimental details.** The experiments were performed on two different scanning tunneling microscopes (STM) operating in ultra-high vacuum. A commercial JT STM (from specs) operated at 1.2 K with a magnetic field up to 3 Tesla was used to measure the temperature and magnetic field dependence of the Kondo resonance, while other experiments were done with a home made STM operating at 5 K. Both setups allow in situ sample preparation and transfer into the STM. The Au(111) substrate was cleaned in UHV by repeated cycles of Ne<sup>+</sup> ion sputtering and subsequent annealing to 730 K. The molecular precursor (2,2'-dibromo-9,9'-bianthracene) was sublimated at 170 °C from a Knudsen cell onto the clean Au(111) substrate kept at room temperature. Then the sample was first annealed at 200 °C for 15 minutes in order to induce the polymerization of the molecular precursors by Ullmann

coupling, then the sample was annealed at 250 °C for 5 minutes to trigger the cyclodehydrogenation to form chiral graphene nanoribbons (chGNRs). A last step annealing at 350 °C for 1 minute created nanostructure junctions. A tungsten tip functionalized with a CO molecule was used for high resolution images. All the images in the manuscript were acquired in constant height mode, at very small voltages, and junction resistances of typically 20 M $\Omega$ . The  $dI/dV$  signal was recorded using a lock-in amplifier with a bias modulation of  $V_{\text{rms}} = 0.4$  mV at 760 Hz.

**Simulations.** We performed calculations with the SIESTA implementation<sup>38</sup> of density functional theory (DFT). Exchange and correlation (XC) were included within either the local (spin) density approximation (LDA)<sup>39</sup> or the generalized gradient approximation (GGA)<sup>40</sup>. We used a 400 Ry cutoff for the real-space grid integrations and a double-zeta plus polarization (DZP) basis set generated with an 0.02 Ry energy shift for the cutoff radii. The molecules, represented with periodic unit cells, were separated by a vacuum of at least 10 Å in any direction. The electronic density was converged to a stringent criterion of  $10^5$ . The force tolerance was set to 0.002 eV/Å. Here is a description of a specific method used. To complement the DFT simulations described above we also performed simulations based on the mean-field Hubbard (MFH) model, known to provide a good description for carbon  $\pi$ -electron systems<sup>7,8,15,16,41</sup>.

**Acknowledgements** We thank Manuel Vilas-Varela for the synthesis of the chGNR molecular precursor. We are indebted to Carmen Rubio, Dimas G. de Oteyza, Nestor Merino, Nicolás Lorente, Aran García Lekue, and Daniel Sánchez Portal for fruitful discussions.

We acknowledge financial support from Spanish AEI (MAT2016-78293-C6, FIS2017-83780-P, and the Maria de Maeztu Units of Excellence Programme MDM-2016-0618), the Basque Government (Dep. Industry, Grant PI-2015-1-42), the EU project PAMS (610446), the Xunta de Galicia (Centro singular de investigación de Galicia accreditation 2016-2019, ED431G/09), and the European Regional Development Fund (ERDF).

**Author Contributions** J.L. and J.I.P. devised the experiment. D.P. designed the organic synthesis of



the chGNR molecular precursor. J.L. realized the measurements. S.S. and T.F. did the theoretical simulations. All the authors discussed the results. J.L., T.F., and J.I.P. wrote the manuscript.

**Competing Interests** The authors declare that they have no competing financial interests.

# Supplementary Information for: Single Spin Localization and Manipulation in Graphene Open-Shell Nanostructures

Jingcheng Li<sup>1</sup>, Sofia Sanz<sup>2</sup>, Martina Corso<sup>2,3</sup>, Deung Jang Choi<sup>2,3,5</sup>, Diego Peña<sup>4</sup>, Thomas Frederiksen<sup>2,5</sup> & Jose Ignacio Pascual<sup>1,5</sup>

<sup>1</sup>*CIC nanoGUNE, 20018 Donostia-San Sebastián, Spain*

<sup>2</sup>*Donostia International Physics Center (DIPC), 20018 Donostia-San Sebastián, Spain*

<sup>3</sup>*Centro de Física de Materiales MPC (CSIC-UPV/EHU), 20018 Donostia-San Sebastián, Spain*

<sup>4</sup>*Centro Singular de Investigación en Química Biolóxica e Materiais Moleculares (CiQUS), and Departamento de Química Orgánica, Universidade de Santiago de Compostela, Spain*

<sup>5</sup>*Ikerbasque, Basque Foundation for Science, 48013 Bilbao, Spain April 7, 2024*

## Contents

<b>1</b>	<b>Reaction pathway for the formation of the GNR junctions</b>	<b>2</b>
<b>2</b>	<b>Statistics of different types of junctions</b>	<b>3</b>
<b>3</b>	<b>Understanding the appearance of spins in the junctions from Clar's theory</b>	<b>4</b>
<b>4</b>	<b>Transport spectra of Type 2 junctions</b>	<b>5</b>
<b>5</b>	<b>DFT simulations</b>	<b>6</b>
<b>6</b>	<b>Mean-field Hubbard model</b>	<b>9</b>
<b>7</b>	<b>Singlet-triplet excitations vs molecular size</b>	<b>18</b>
	<b>References</b>	<b>20</b>

## 1 Reaction pathway for the formation of the GNR junctions

Figure S1 shows a plausible mechanism for the formation of the GNR junctions. First, CH activation would form the corresponding sigma-radicals which could evolve by C-C coupling followed by cyclodehydrogenation to obtain a five-membered ring (in red). Then, fragmentation of a benzene ring, followed by H migration could lead to a terminal alkyne (in blue). Finally, isomerization of a double bond, followed by cyclization of the terminal alkyne with a bay region of the GNR, could afford the final GNR junction.

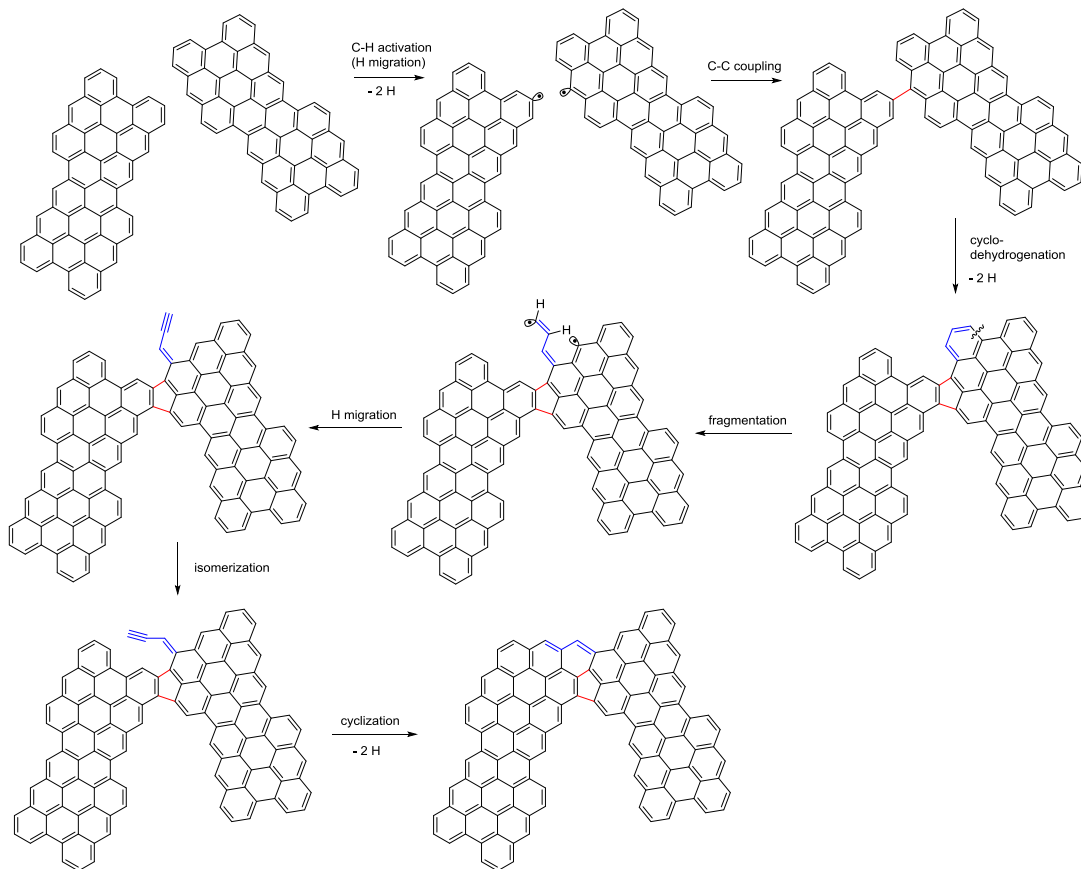


**Figure S1. Proposed reaction pathway for the formation of the graphene nanostructures.**

## 2 Statistics of different types of junctions

In the main text we studied three different nanostructure junctions (Figs. 1 and 2). Here we show the frequency statistics of the three types. From the 45 different junctions studied, 30 of them are identified as Type 3 junctions, while 9 and 5 of them are identified as Type 1 and Type 2 junctions respectively (Figure S2a). From this statistics, we deduced that the ZZ sites are more favorable to incorporate an extra hydrogen atom and get passivated (22% of the radicals). The PC sites had an extra atom only in 13% of the cases. The overall percentage of H-passivation observed here is comparable to the value found at the termination of armchair GNRs [1], which was happened in a 15% of the occasions.

In one of the 45 nanostructures inspected, we observed a junction with same backbone structure as the other three types, but with neither bright sites, nor zero-bias features in the spectra. Figure S2b shows a constant height current image of the junction, where its ring structure can be now nicely resolved. It corresponds to the carbon backbone sketch in Fig. 1d of the main text but with two extra H atoms saturating the radical sites.

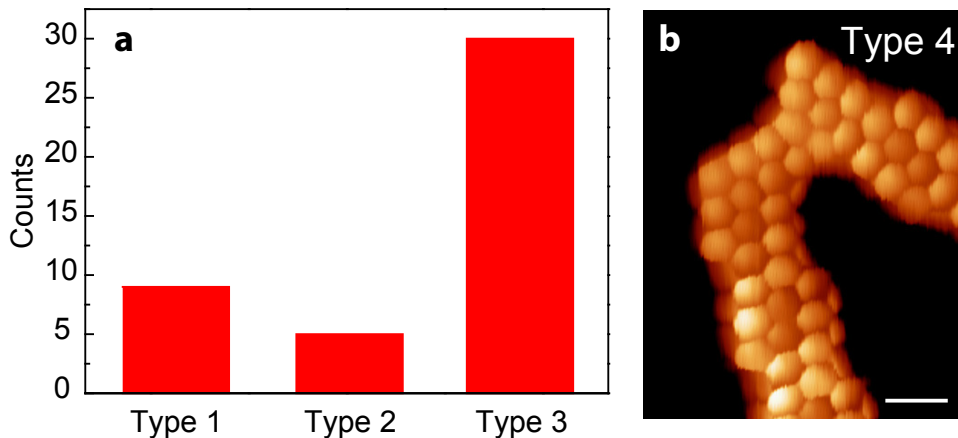


**Figure S2. Statistics of different types of junctions.** a, Bar plot of the number of three types of junctions studied in the main text. b, Constant-height current image ( $V = 2$  mV, scale bar 0.5 nm) shows another type of junctions with both radicals are passivated by H atoms, which is classified as Type 4 junction.

### 3 Understanding the appearance of spins in the junctions from Clar's theory

In the main text, we used both DFT and Hubbard Mean Field simulations to show that the spins in Type 3 junctions comes from two in-gap states, simply occupied as a result of electron-electron correlations. An alternative and intuitive chemical picture behind the emergence of singly occupied radical states can be drawn bearing in mind Clar's aromatic pi-sextet rule [2]. Figure S3 shows two possible resonance structures for the GNR junction: the closed shell structure a, with 8 Clar sextets, and the open shell structure b, with 11 Clar sextets and two radicals at the PC and ZZ sites. The dominance of resonance structure b in our experiments means that the energy required to create the two unpaired electrons (radicals) in structure b is compensated by the stabilization provided by the presence of three additional Clar sextets. In fact, the radical sites can delocalize towards the two second neighbor edge carbon atoms, agreeing with the carbon sites with high density of states shown in Fig. 1e in the main text. Hence, this phenomenological model can qualitatively explain the spontaneous appearance of spin in the nanostructures.

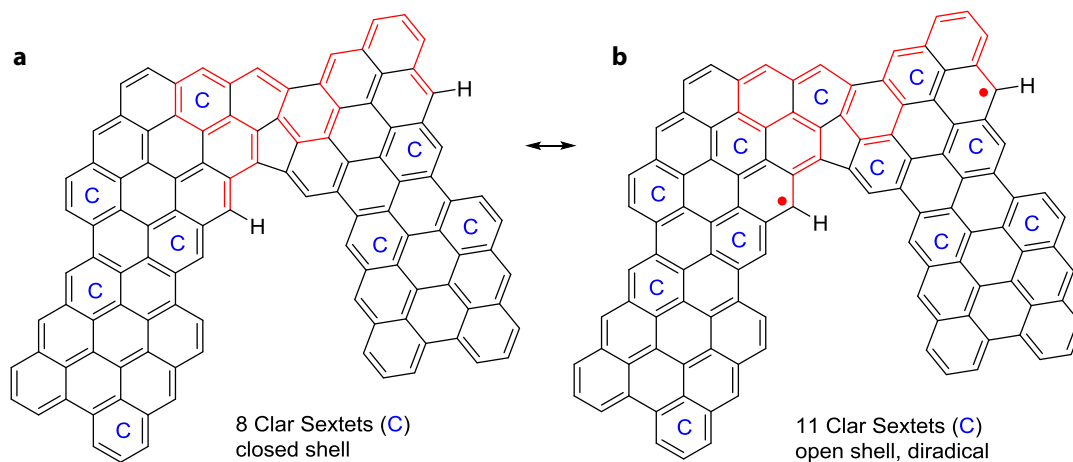


**Figure S3. Understanding the appearance of spins in the nanostructures from Clar's theory.** a, Close-shell resonant structure of a Type 3 nanostructure, with its Clar's sextets indicated with "c". b, Di-radical form of the model structure in a, hosting three additional sextets. Only the H atom of the sites becoming radicals is shown in this model. Structure b is the energetically most stable if the energy gain by incorporating the additional sextets compensates the energy cost for creating the pair of radicals. In this case, the di-radical form is expected to show spin-polarization at the radical sites.

## 4 Transport spectra of Type 2 junctions

In Fig. 5 of the main text, we studied the behaviour of a spin localized at the PC site in a transport measurement, when a Type 3 junction was contacted with the STM tip at the neighbour ZZ site and lifted. Electrons injected through the conjugated backbone reproduced the Kondo resonance observed in tunneling regime. For comparison, here we show similar transport measurement for a Type 2 junction, i.e. when there is no spin in the graphene nanostructure. As in the other case, the STM tip was approached to the radical at the ZZ site to make a bond between nanostructure and STM tip (illustrated in Figure S4). Before bond formation, the characteristic Kondo resonance of Type 2 junctions is observed in the  $dI/dV$  spectra (point 1 in the figure). However, once the radical bonded to the tip (signalled by the characteristic jump-to-contact step), the junction bridged tip and substrate and the Kondo resonance disappeared. This proves that the tip-radical contact quenches the magnetic moment of this site, as presumed in Fig. 5. It also proves that the Kondo feature observed in Fig. 5 for the lifted junction correspond to the PC spin embedded in the cGNR junction.

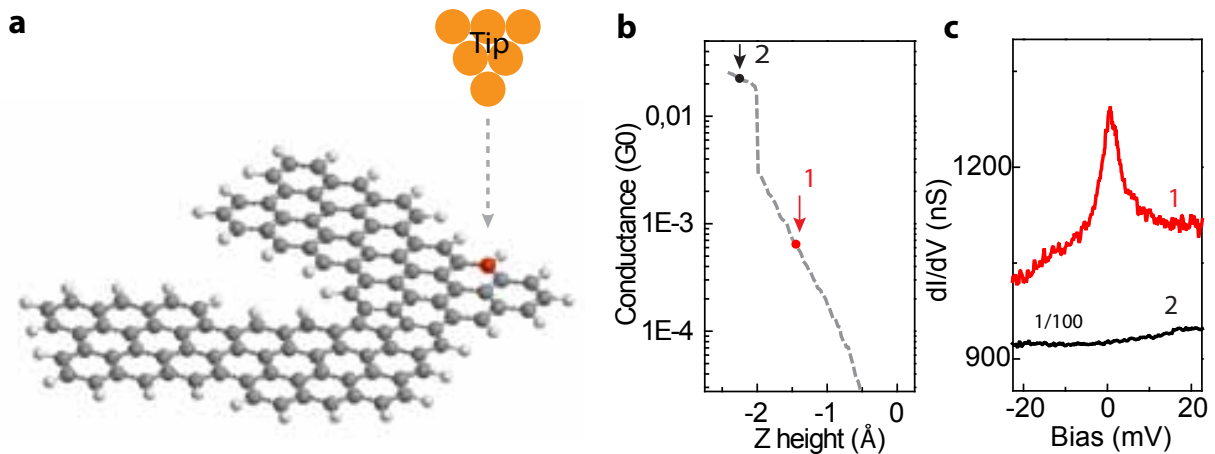


**Figure S4. Transport properties of the lifted junctions without radical.** a, Schema illustrating the process, when the STM tip was approached to the ZZ radical of a Type 2 junction (gray dashed arrow) to form a contact. b, Simultaneously recorded conductance curve ( $V = -50$  mV) during the process in a. Red and black dots indicate the vertical positions at which  $dI/dV$  spectra in c were taken.

## 5 DFT simulations

We performed calculations with the SIESTA implementation [3] of density functional theory (DFT). Exchange and correlation (XC) were included within either the local (spin) density approximation (LDA) [4] or the generalized gradient approximation (GGA) [5]. We used a 400 Ry cutoff for the real-space grid integrations and a double-zeta plus polarization (DZP) basis set generated with an 0.02 Ry energy shift for the cutoff radii. The molecules, represented with periodic unit cells, were separated by a vacuum of at least 10 Å in any direction. The electronic density was converged to a stringent criterion of  $10^5$ . The force tolerance was set to 0.002 eV/Å. In Fig. 3 in the main text we report the GGA results.

**Role of exchange-correlation functional** In Figure S5 we compare the calculated spin polarization for the generic (2,2) graphene nanojunction within both LDA [4] and GGA [5] XC approximations. We also compare the real-space spin density with a Mulliken population analysis. From Figure S5 it is clear that the emerging picture for the radicals is robust among all four approaches. As expected, the intensity of the spin polarization is more pronounced in GGA than in LDA.

**Energetically preferred hydrogen passivation sites** In the main text we showed the hydrogen passivation on ZZ sites (Type 1 junctions) and PC sites (Type 2 junctions). In Figure S2 we report a higher probability of hydrogen passivation on ZZ sites than PC sites. To quantitatively study this phenomenon, we analysed the energetics of different hydrogen passivations of the edges from DFT simulations. The results are summarized in Figure S6. We find that hydrogen passivation on the ZZ and PC sites are indeed the two most stable configurations, with the former being the energetically most favoured one. This is in agreement with the experimental observations (Figure S2).

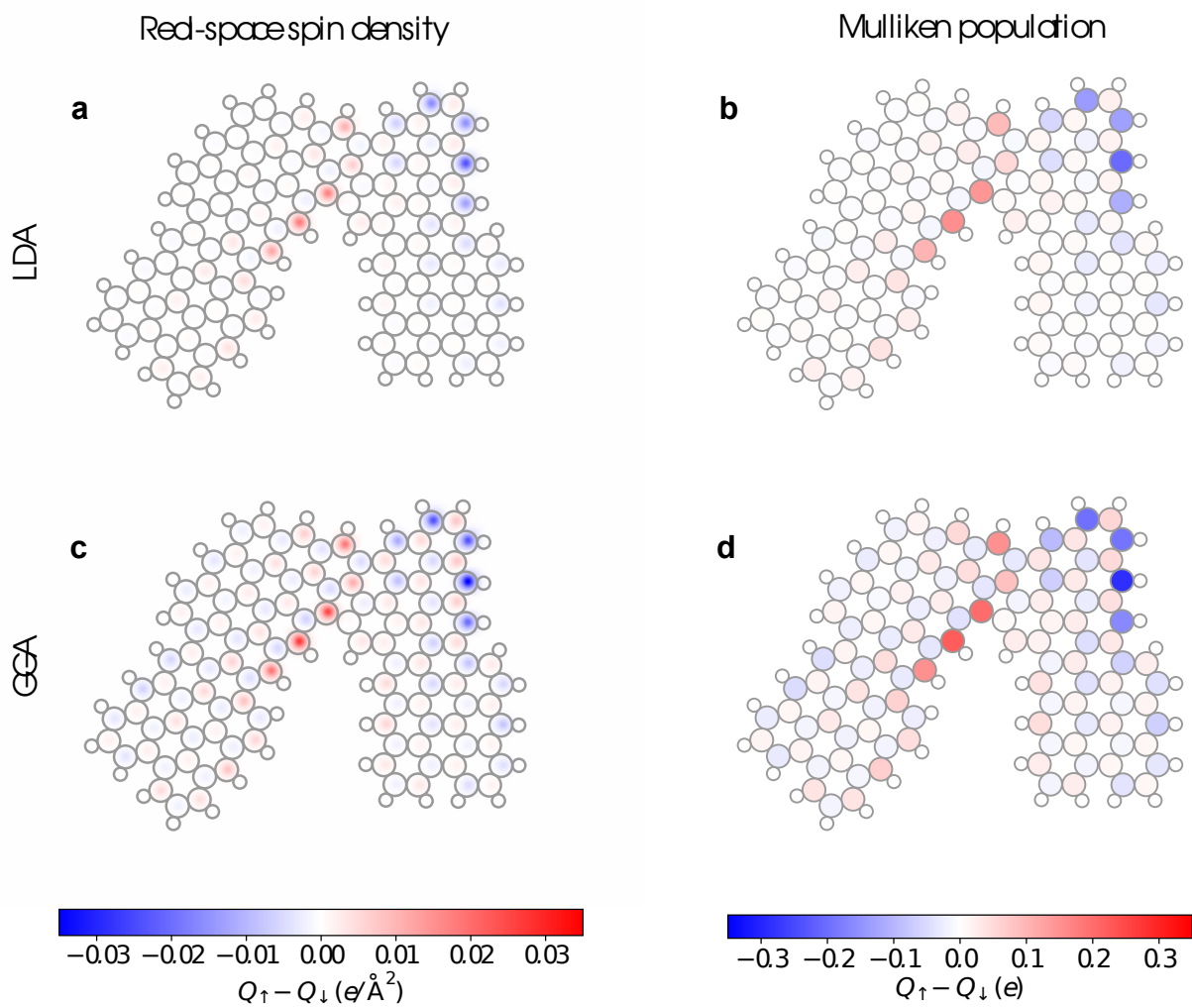


**Figure S5. Spin polarization in the (2,2)-junction from DFT simulations.** a, Real-space spin density calculated within LDA. b, Mulliken population analysis of the spin density calculated within LDA. c,d Same as a,b but for GGA. Panel d corresponds to Fig. 3a in the main text.



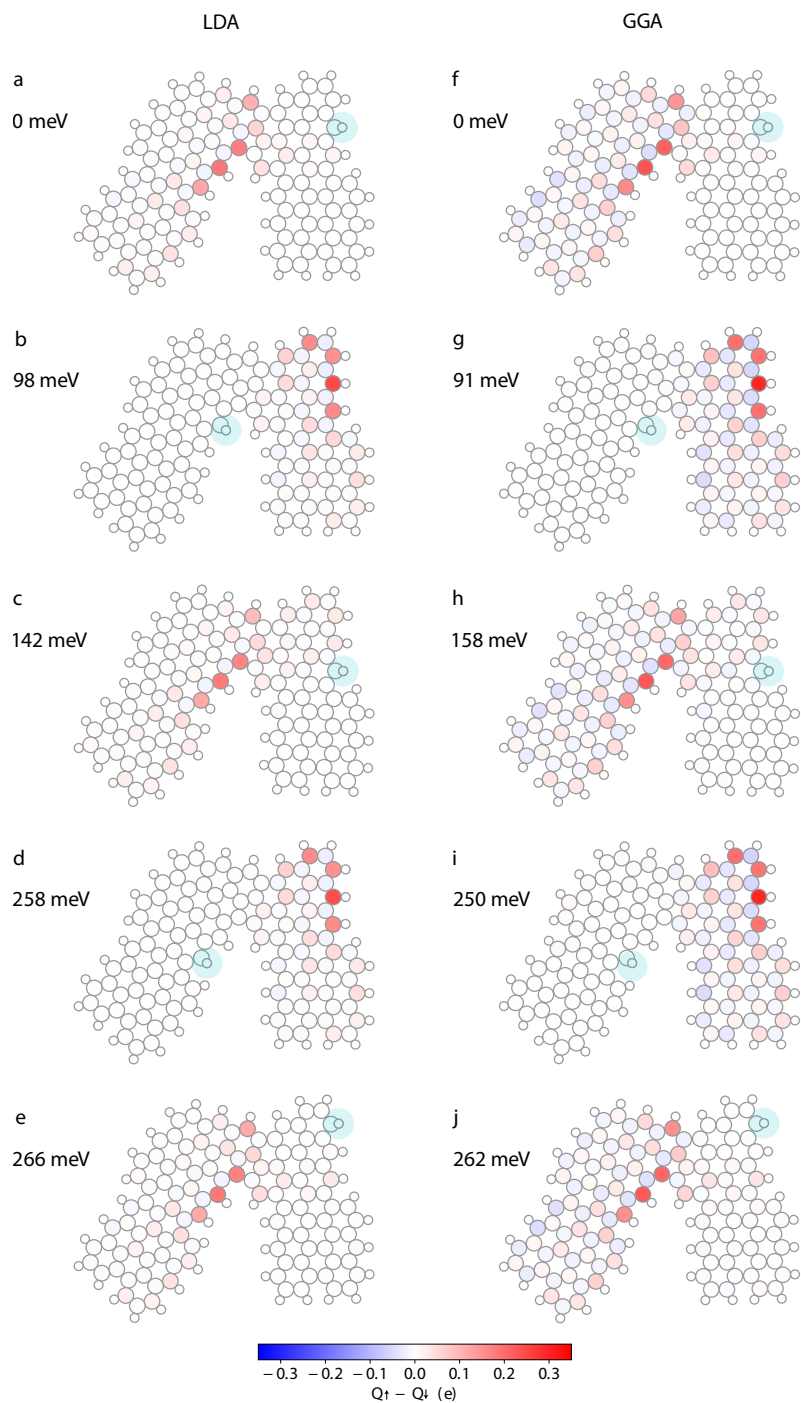


**Figure S6. Energetics and spin polarization for five energetically preferred hydrogen passivation sites from DFT simulations.** a-e, Results from LDA calculations via a Mulliken population analysis. The hydrogen passivation (blue circles) shown in a on the ZZ site is the most stable configuration, while the other sites are less energetically favoured with the energy differences quoted in each panel. f-j, Same molecules as in a-e but results from GGA calculations. Panels f,g correspond to Fig. 3b in the main text.

## 6 Mean-field Hubbard model

To complement the DFT simulations described above we also performed simulations based on the mean-field Hubbard (MFH) model, known to provide a good description for carbon  $\pi$ -electron systems [6–10]. We describe the graphene nanostructures with the following Hamiltonian for the  $sp^2$  carbon atoms:

$$\begin{aligned}
 H = & -t_1 \sum_{\langle i,j \rangle, \sigma} (c_{i\sigma}^\dagger c_{j\sigma} + \text{h.c.}) - t_2 \sum_{\langle\langle i,j \rangle\rangle, \sigma} (c_{i\sigma}^\dagger c_{j\sigma} + \text{h.c.}) - t_3 \sum_{\langle\langle\langle i,j \rangle\rangle\rangle, \sigma} (c_{i\sigma}^\dagger c_{j\sigma} + \text{h.c.}) \\
 & + U \sum_i (n_{i\uparrow} \langle n_{i\downarrow} \rangle + \langle n_{i\uparrow} \rangle n_{i\downarrow} - \langle n_{i\uparrow} \rangle \langle n_{i\downarrow} \rangle)
 \end{aligned} \tag{1}$$

where  $c_{i\sigma}$  ( $c_{i\sigma}^\dagger$ ) annihilates (creates) an electron with spin  $\sigma$  in the  $p_z$  orbital centred at site  $i$ . The first three terms describe a tight-binding model with hopping amplitudes  $t_1$ ,  $t_2$ , and  $t_3$  for the first, second, and third-nearest neighbour matrix elements (defined in terms of interatomic distances  $d_1 < 1.6\text{\AA} < d_2 < 2.6\text{\AA} < d_3 < 3.1\text{\AA}$ ). We follow the parameterizations of Ref. [10] and consider both a simple first-nearest neighbour (1NN) model with  $t_1 = 2.7$  eV and  $t_2 = t_3 = 0$  as well as a more accurate third-nearest neighbour (3NN) model with  $t_1 = 2.7$  eV,  $t_2 = 0.2$  eV, and  $t_3 = 0.18$  eV.

The term proportional to the empirical parameter  $U$  accounts for the on-site Coulomb repulsion. By comparison with first-principles simulations it has been established that DFT-GGA (DFT-LDA) are generally best reproduced when  $U/t \approx 1.3$  (0.9) [8]. Consistent with this, we find a good overall agreement with our experimental observations using  $U \sim 3.5$  eV as analysed below.

The expectation value of the spin-resolved density operator  $n_{i\sigma} = c_{i\sigma}^\dagger c_{i\sigma}$  is computed from the eigenvectors of  $H$ . From the self-consistent solution of the Hamiltonian in Eq. (1) we obtain the local spin density from the charge difference  $Q_{i\uparrow} - Q_{i\downarrow}$ , with  $Q_{i\sigma} = e \langle n_{i\sigma} \rangle$ . In units of  $\mu_B$  the magnetization is  $M_i = (n_{i\uparrow} - n_{i\downarrow})/2$ .

We solve the mean-field Hubbard model using a custom-made Python implementation based on SISL [11]. In Fig. 3 in the main text we report the non-interacting single-particle wave functions in the 3NN model ( $U = 0$ ) as a basis to understand the open-shell electronic configurations obtained in DFT and MFH.

**Band structure of infinite (3,1)cGNRs** As shown in Figures. S7 and S8, both the first-neighbour and third-neighbour MFH models (red bands) provide a good description for the 1D band structure of the (3,1) chiral graphene nanoribbon (cGNR) as compared to DFT calculations (black bands) obtained with SIESTA [3]. Unlike DFT and the 3NN model, the simple 1NN model implies electron-hole symmetry of the bands. The low-energy part of the DFT band structure is generally very well reproduced with MFH using an on-site Coulomb repulsion of  $U \leq 3.5$  eV. Indeed this narrow cGNR is intrinsically non-magnetic, consistent with previous works [8, 9, 12].

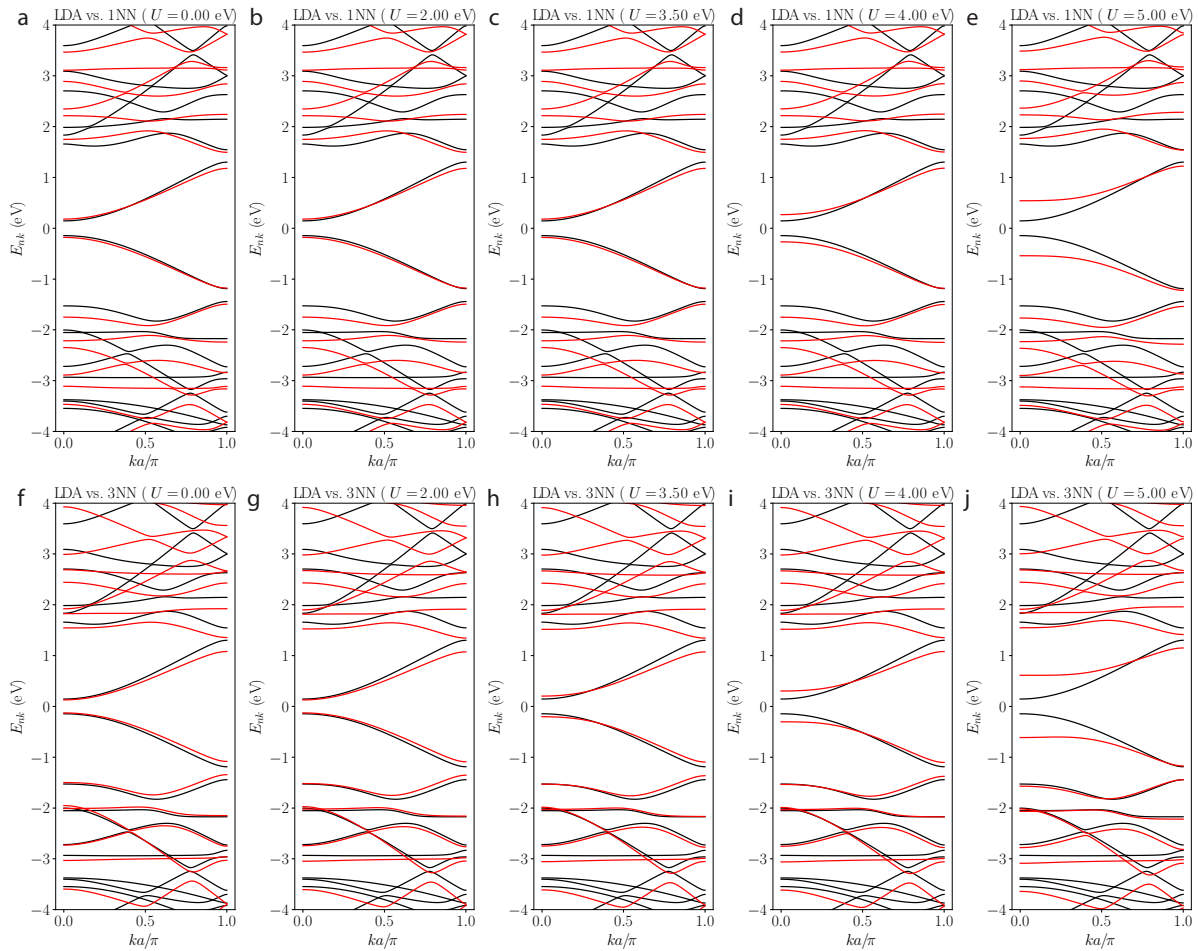


**Figure S7. Calculated 1D band structure for the (3,1)cGNR.** We compare DFT-LDA (black lines) with the mean-field Hubbard model with different Coulomb repulsion  $U$  (red lines) within either **(a-e)** first-nearest neighbour couplings only ( $t_1 = 2.70$  eV, top row) or **(f-j)** third-nearest neighbour couplings ( $t_1 = 2.70$  eV,  $t_2 = 0.20$  eV, and  $t_3 = 0.18$  eV, bottom row).

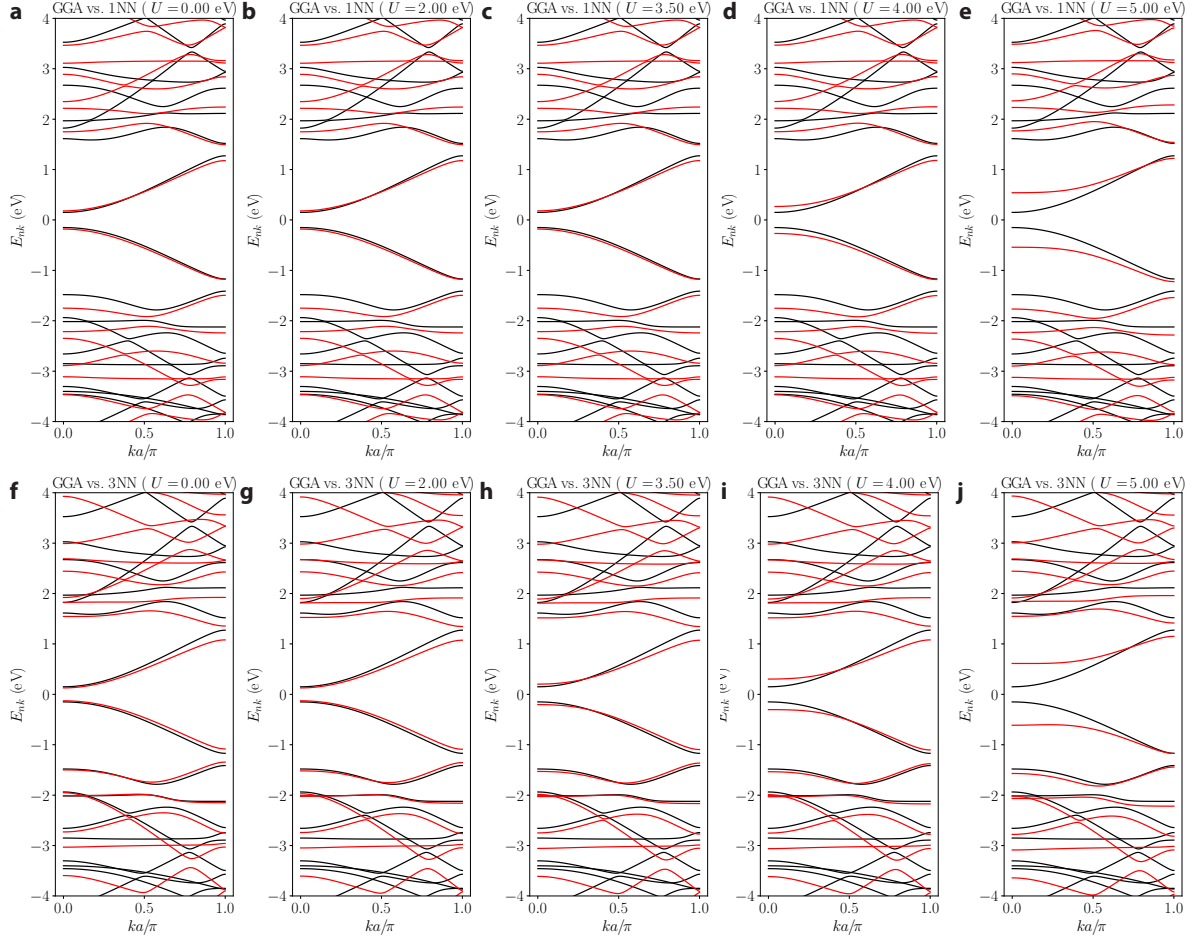


**Figure S8. Calculated 1D band structure for the (3,1)cGNR.** We compare DFT-GGA (black lines) with the mean-field Hubbard model with different Coulomb repulsion  $U$  (red lines) within either **(a-e)** first-nearest neighbour couplings only ( $t_1 = 2.70$  eV, top row) or **(f-j)** third-nearest neighbour couplings ( $t_1 = 2.70$  eV,  $t_2 = 0.20$  eV, and  $t_3 = 0.18$  eV, bottom row).

**Spin polarization** In Figure S9 we examine the spatial spin density obtained with MFH for both 1NN and 3NN models and varying on-site Coulomb repulsion. In the 1NN (3NN) model the onset of spin polarization occurs around  $U = 3.1$  (2.7) eV. Compared with the DFT results in Figure S5 (and the band structures of the previous section) we conclude that the 3NN model with Coulomb repulsion of the order  $U = 3.5$  eV yields a very satisfactory agreement with DFT.

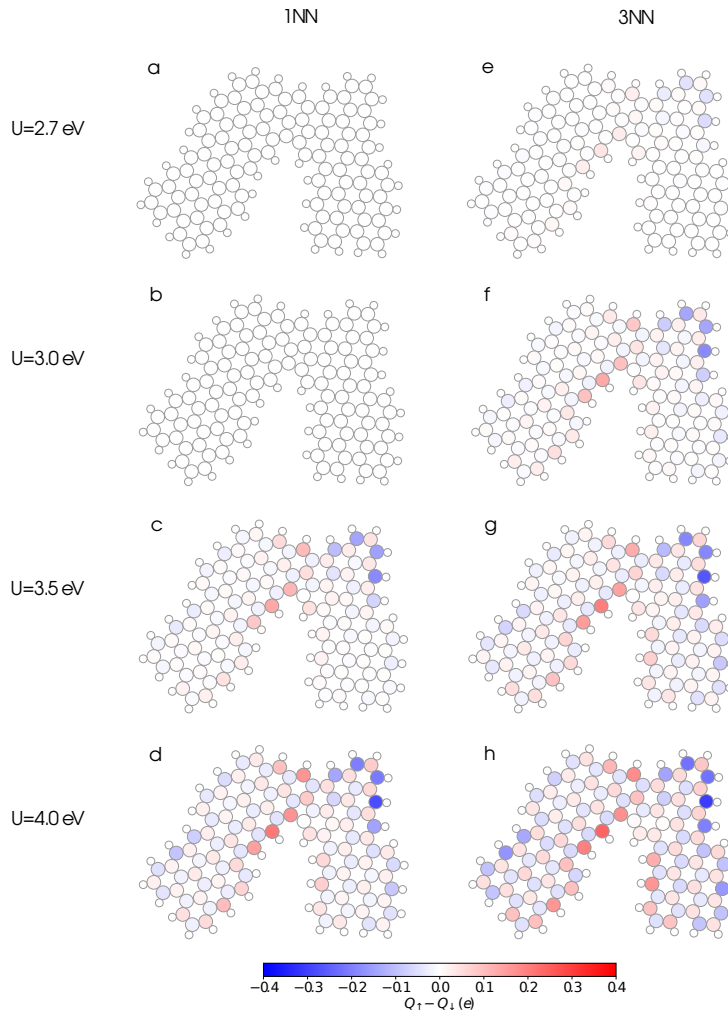


**Figure S9. Spin density from MFH calculations.** (a-d) Spatial spin density, computed at site  $i$  as  $Q_{i\uparrow} - Q_{i\downarrow}$ , for different values of the on-site Coulomb repulsion parameter  $U$ . (e-h) Same as (a-d) but for the 3NN model.

**Single-particle wave functions** In Figure S10 and Figure S11 we analyze the eigenspectrum of energies and states in both the non-interacting ( $U = 0$ ) and interacting ( $U = 3.5$  eV) MFH Hamiltonians. The degree of spatial localization of each state is computed as  $\eta_{\alpha\sigma} = \int dr |\psi_{\alpha\sigma}|^4$ , also denoted the inverse participation ratio [13]. The HOMO/LUMO wave functions, shown in Figure S12 for  $U = 0$  and in Figure S13 for  $U = 3.5$  eV, are concentrated around the radical sites of the structure.

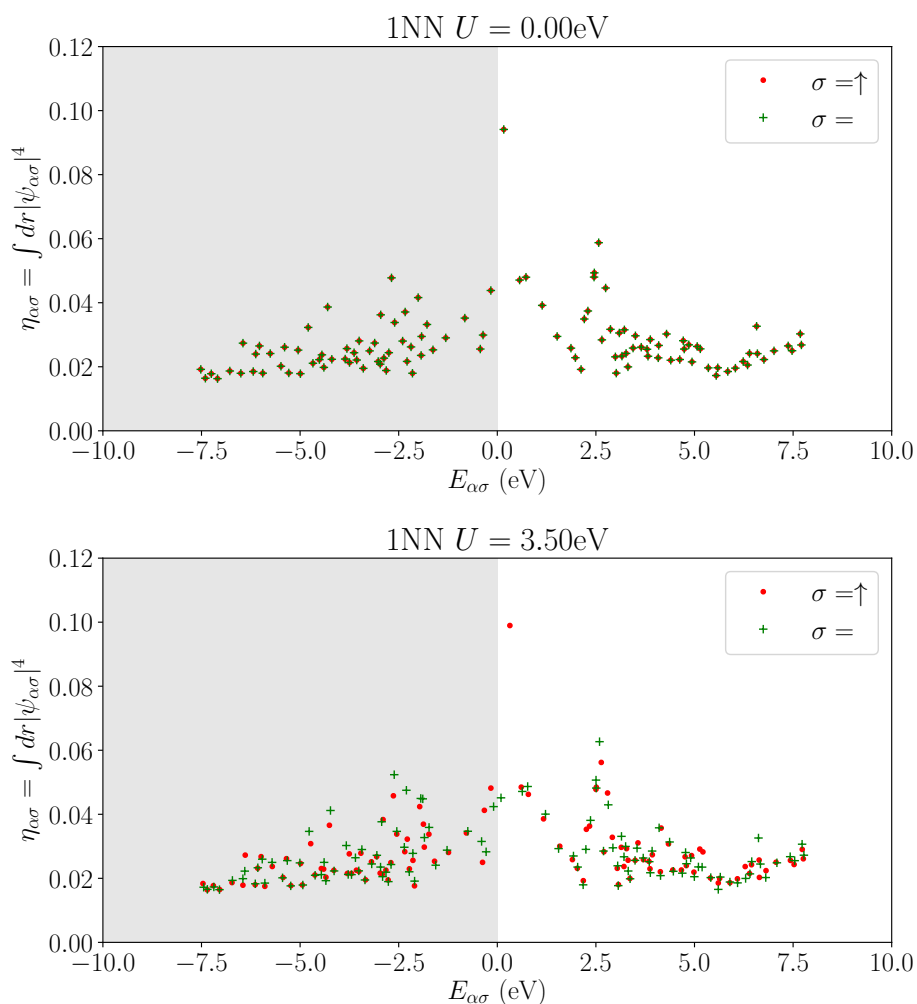


**Figure S10. Single-particle orbital localization  $\eta_{\alpha\sigma}$  versus single-particle energy  $E_{\alpha\sigma}$  in the 1NN model.** Here we consider two characteristic values of  $U$  in both the 1NN and 3NN TB models. Among all states the LUMO orbital ( $\sigma = \uparrow$  for finite  $U$ ) is the most localized one.

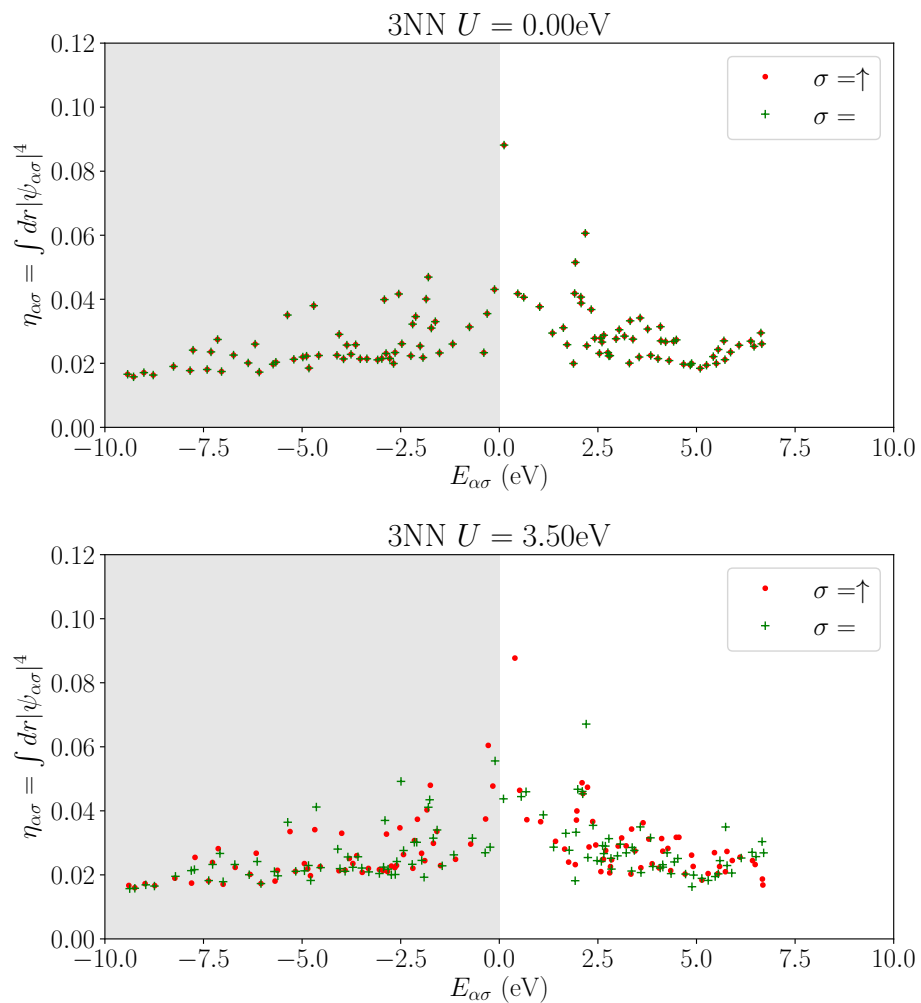


**Figure S11. Single-particle orbital localization  $\eta_{\alpha\sigma}$  versus single-particle energy  $E_{\alpha\sigma}$  in the 3NN model.** Here we consider two characteristic values of  $U$  in both the 1NN and 3NN TB models. Among all states the LUMO orbital ( $\sigma = \uparrow$  for finite  $U$ ) is the most localized one.

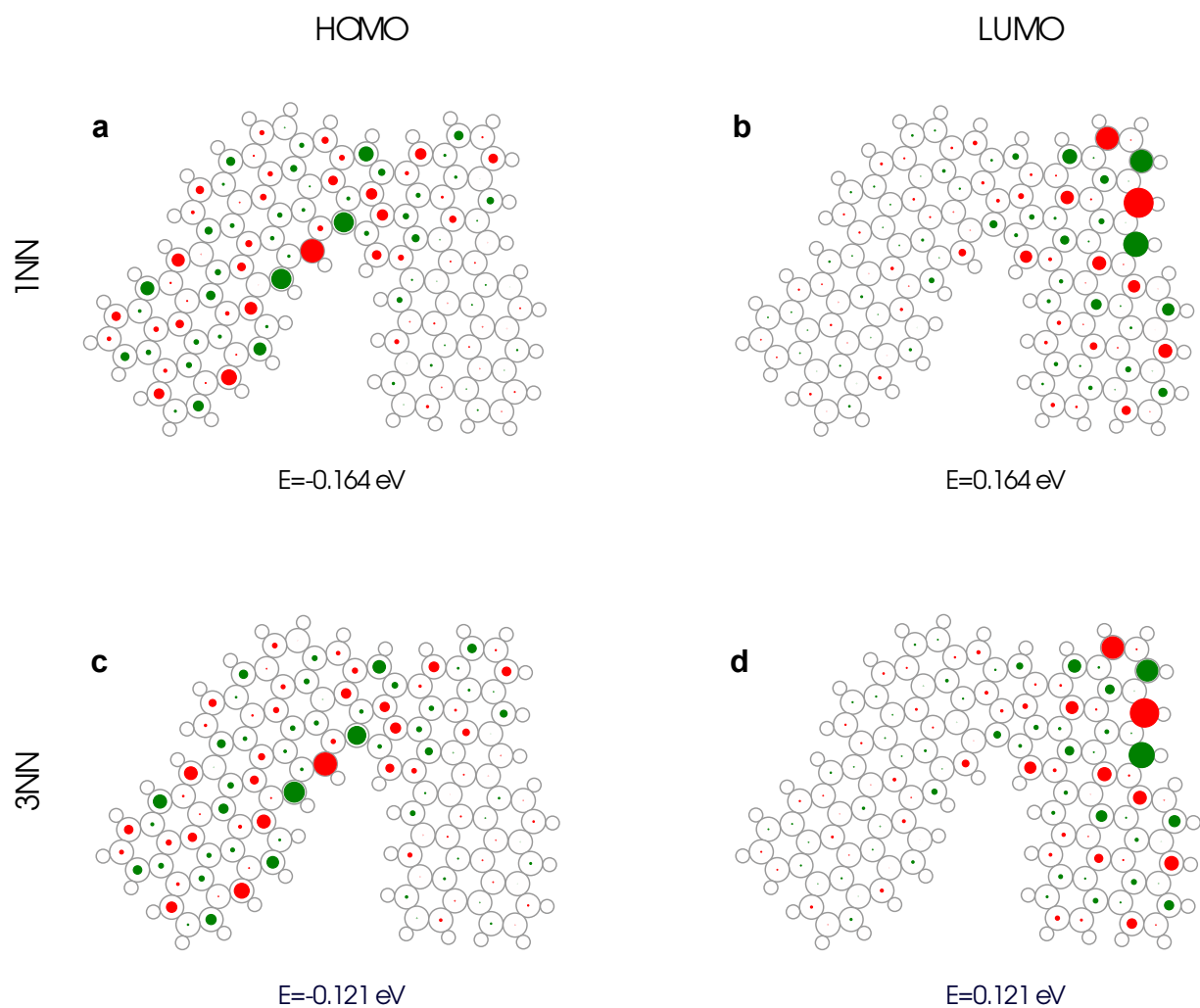


**Figure S12. Single-particle wave functions from MFH with  $U = 0$  eV.** a,b, Spatial distribution of the HOMO and LUMO wave functions within the 1NN model. c,d, Same as a,b but within the 3NN model. Panels c,d correspond to Fig. 3e in the main text. The single-particle energies relative to the midgap are stated below each plot. The size and color of the red-green circles reflect magnitude and phase of the wave function coefficients on each carbon atom, respectively.



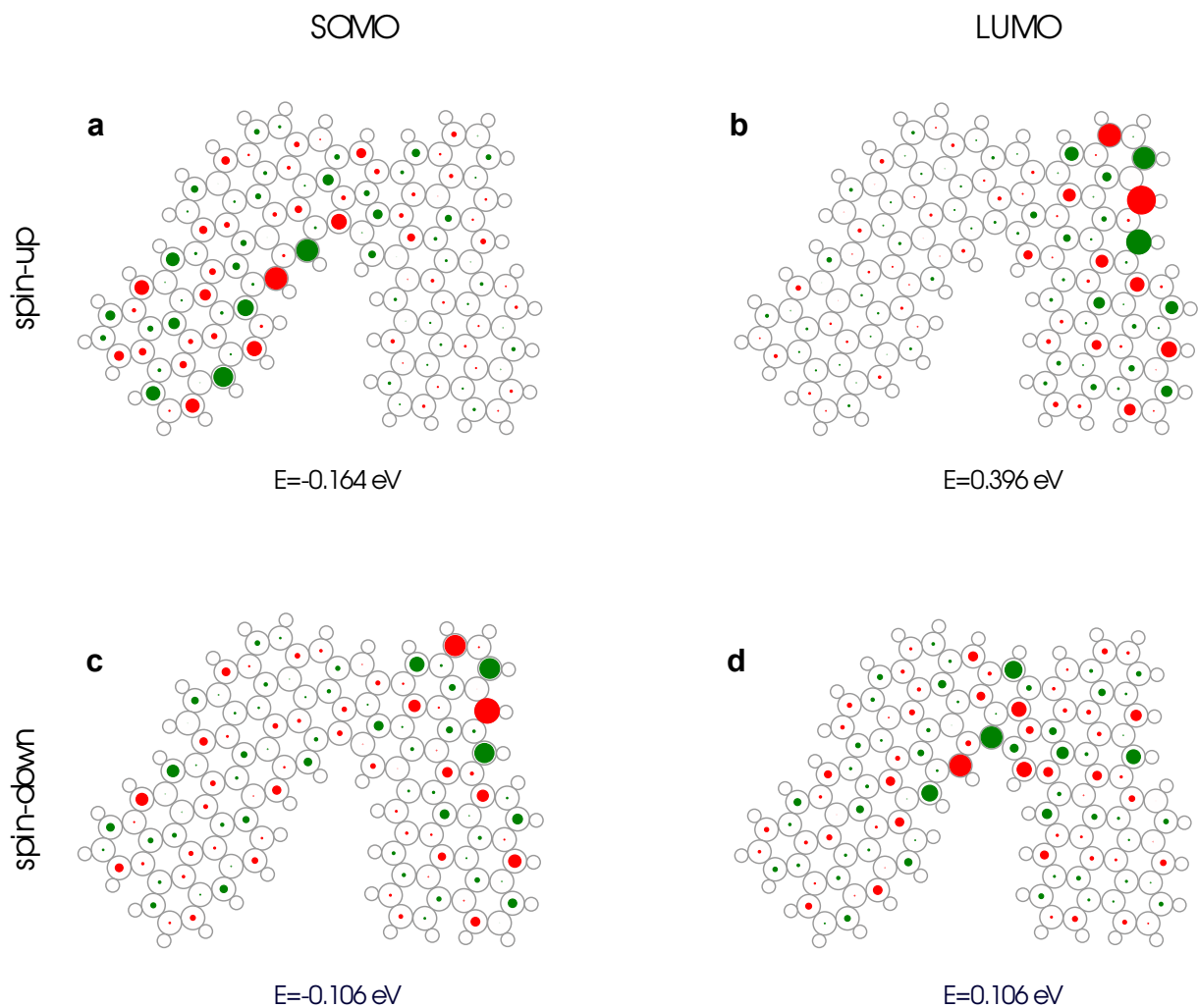


**Figure S13. Single-particle wave functions from MFH within the 3NN model with  $U = 3.5$  eV.** a,b, Spatial distribution of the SOMO and LUMO wave functions for the spin-up electrons, respectively. c,d, Same as a,b but for the spin-down electrons. The single-particle state energies relative to the midgap are stated below each plot. The size and color of the red-green circles reflect magnitude and phase of the wave function coefficients on each carbon atom, respectively.

**Singlet-triplet excitations** From Figure S9 we have established that  $U = 3.5$  eV yields a good description for these nanostructures as compared with DFT. As an approximation to the true singlet-triplet excitation energy  $J$ , we computed the mean-field energy difference  $\Delta E_{ST}$  between the converged electronic configurations with  $n_{\uparrow} = n_{\downarrow}$  and  $n_{\uparrow} = n_{\downarrow} + 2$ . In Figure S14 we explore the variation of  $\Delta E_{ST}$  with  $U$  for a Type 3 junction. Within the 3NN model a minimum is observed close to  $\Delta E_{ST} \sim 19$  meV at  $U \sim 3.5$  eV, in reasonable agreement with (albeit larger than) the experimentally observed peak splitting.

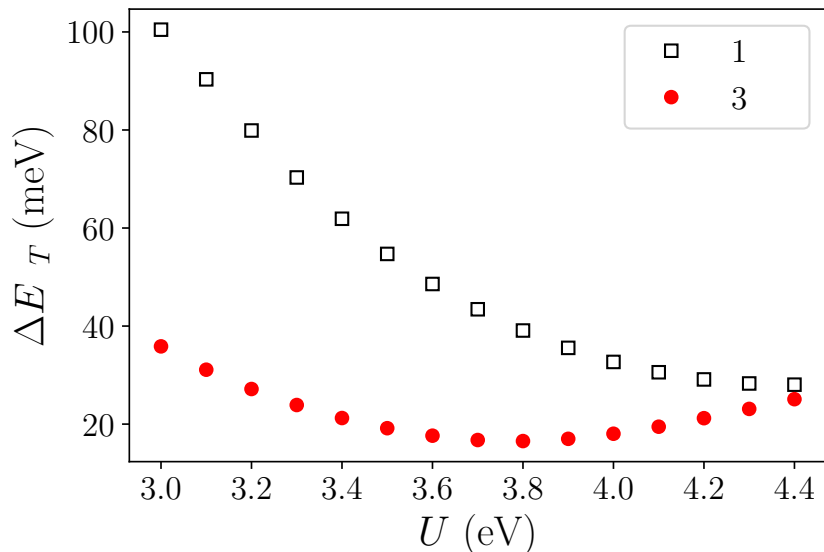


**Figure S14. Singlet-triplet excitation energy  $\Delta E_{ST}$  versus  $U$ .** We consider here the prototype molecule  $(L, R) = (2, 2)$  within both the 1NN and 3NN models. The curves increase monotonically to the HOMO-LUMO gap  $\Delta E_{H-L} = 0.328$  (0.242) eV in the limit  $U \rightarrow 0$  for the 1NN (3NN) model.

## 7 Singlet-triplet excitations vs molecular size

In the main text we have shown that the singlet-triplet excitation energy of Type 3 junctions decreases with the size of the junctions, namely, with the length of the contacted ribbons. Here, we present results of the interaction energy between two coupled spins for several junctions, which corroborate this dependence.

In Figure S15b we report experimentally extracted values of the singlet-triplet excitation energy from fits of a set of junctions, all with a similarly long arm  $a$ , as a function of the length of arm  $b$ . When the arm  $b$  consists of two precursor units, the singlet-triplet excitation energy is relatively low (below 3 meV), but for larger length of  $b$  (more than three precursor units) the energy difference raises quickly to around 8 meV. This trend is confirmed by the MFH simulations (Figure S15c,d) both with the first-nearest hopping model (1NN) and the third-nearest hopping model (3NN). However, the experimental values are smaller than the computed ones. The origin of this could be related to the presence of a metal surface in the experiment, to the approximation of having only local Coulomb repulsion in the theory, or to limitation of the meanfield description.

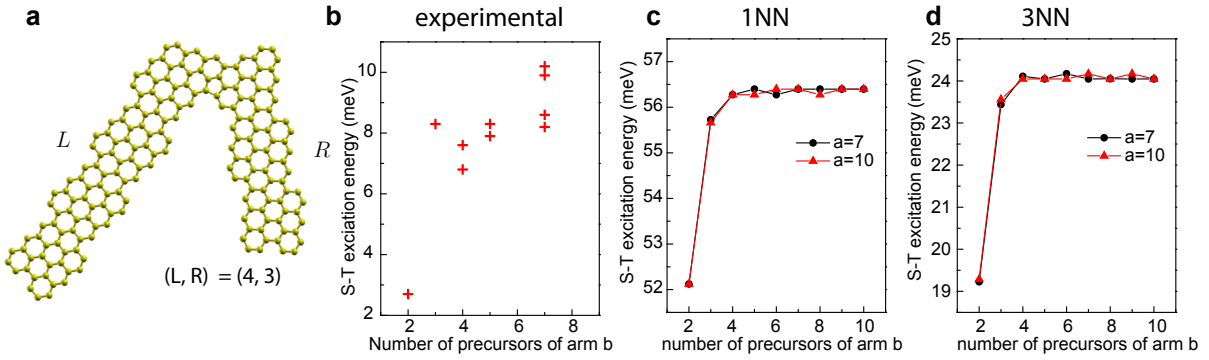


**Figure S15. Size-dependent singlet-triplet excitation energy of Type 3 junctions.** a, Backbone structure of a Type 3 junction to illustrate how the size of a junction is measured in terms of the number of precursor units of each of its arms (defined as arm  $L$  and  $R$  as in the main text). b, Experimentally obtained spin-spin coupling energy  $J$  plotted as a function of the length of arm  $R$ . All junctions had arm  $L > 7$ . Each data point was extracted from a fit of  $dI/dV$  spectra as described in Fig. 2f. c, Calculated excitation energies as a function of the length of arm  $R$  within MFH with  $U = 3.5$  eV in the first-nearest hopping model (1NN). Here the length of arm  $a$  are fixed as 7 and 10, respectively. d, Same as c but for the third-nearest hopping model (3NN).

1. Talirz, L *et al.*, Termini of Bottom-Up Fabricated Graphene Nanoribbons, *J. Am. Chem. Soc.*, **135**, 2060-2063 (2013)
2. Solà, M., Forty years of Clar's aromatic -sextet rule, *Front. Chem.* **1**, 22 (2013).
3. Soler, J. M. *et al.* The siesta method for ab initio order-n materials simulation. *J. Phys.: Condens. Matter* **14**, 2745–2779 (2002).
4. Ceperley, D. M. & Alder, B. J. Ground state of the electron gas by a stochastic method. *Phys. Rev. Lett.* **45**, 566–569 (1980).
5. Perdew, J. P., Burke, K. & Ernzerhof, M. Generalized gradient approximation made simple. *Phys. Rev. Lett.* **77**, 3865–3868 (1996).
6. Fernández-Rossier, J. & Palacios, J. J. Magnetism in Graphene Nanoislands. *Phys. Rev. Lett.* **99**, 177204 (2007).
7. Yazyev, O. V. Emergence of magnetism in graphene materials and nanostructures. *Rep. Prog. Phys.* **73**, 056501 (2010).
8. Yazyev, O. V., Capaz, R. B. & Louie, S. G. Theory of magnetic edge states in chiral graphene nanoribbons. *Phys. Rev. B* **84**, 115406 (2011).
9. Carvalho, A. R., Warnes, J. H. & Lewenkopf, C. H. Edge magnetization and local density of states in chiral graphene nanoribbons. *Phys. Rev. B* **89**, 245444 (2014).
10. Hancock, Y., Uppstu, A., Saloriutta, K., Harju, A. & Puska, M. J. Generalized tight-binding transport model for graphene nanoribbon-based systems. *Phys. Rev. B* **81**, 245402 (2010).
11. Papior, N. R. sisl: v0.9.2. <https://github.com/zerothi/sisl/>.
12. Merino-Díez, N. *et al.* Unraveling the electronic structure of narrow atomically precise chiral graphene nanoribbons. *J. Phys. Chem. Lett.* **9**, 25–30 (2018).
13. Ortiz, R., García-Martínez, N. A., Lado, J. L. & Fernández-Rossier, J. Electrical spin manipulation in graphene nanostructures. *arXiv:1712.97282v1*.